

# Blind as a bat: audible echolocation on small robots

Frederike Dümbsgen   Adrien Hoffet   Mihailo Kolundžija   Adam Scholefield   Martin Vetterli

**Abstract**—For safe and efficient operation, mobile robots need to perceive their environment, and in particular, perform tasks such as obstacle detection, localization, and mapping. Although robots are often equipped with microphones and speakers, the audio modality is rarely used for these tasks. Compared to the localization of sound sources, for which many practical solutions exist, algorithms for active echolocation are less developed and often rely on hardware requirements that are out of reach for small robots.

We propose an end-to-end pipeline for sound-based localization and mapping that is targeted at, but not limited to, robots equipped with only simple buzzers and low-end microphones. The method is model-based, runs in real time, and requires no prior calibration or training. We successfully test the algorithm on the *e-puck* robot with its integrated audio hardware, and on the *Crazyflie* drone, for which we design a reproducible audio extension deck. We achieve centimeter-level wall localization on both platforms when the robots are static during the measurement process. Even in the more challenging setting of a flying drone, we can successfully localize walls, which we demonstrate in a proof-of-concept multi-wall localization and mapping demo.

**Index Terms**—Range Sensing, Robot Audition, SLAM, Aerial Systems: Perception and Autonomy

## I. INTRODUCTION

A bat’s ability to “see” in the dark using sound has fascinated scientists for centuries [1]. Bats emit ultrasonic chirps, and based on the timing and form of the echoes, localize objects of interest such as food [2], obstacles [3], or water resources [4].

Similarly, most mobile robots need to localize targets and obstacles in their surroundings in order to perform meaningful operations such as search and rescue, exploration, and delivery. Most robots that are currently deployed in the real world rely on rich sensors for localization and mapping — sensors that provide a plethora of information — such as cameras, lidar [5] or radar [6].

However, just like bats have relatively poor eyesight, not all robots can be equipped with rich sensing equipment. Consider the *Crazyflie*, a developer-friendly nano drone [7]. This drone is very limited in terms of admissible payload, which rules out heavy sensors such as lidar or radar. A single camera can be attached through the *AI-deck*; however, this does not provide full coverage for obstacle avoidance. More coverage can be obtained with the *multi-ranger deck*, designed specifically for obstacle detection using four infrared sensors.

We propose to instead use audible sound for obstacle detection and mapping. Microphones come in lighter and smaller

This work was supported in part by “SNF-SESAM – Sensing and Sampling: Theory and Algorithms.” n° 200021\_181978/1.

All authors are with the School of Computer and Communication Sciences, EPFL, 1015 Lausanne, Switzerland. Corresponding author: Frederike Dümbsgen, [frederike.duembsgen@gmail.com](mailto:frederike.duembsgen@gmail.com).

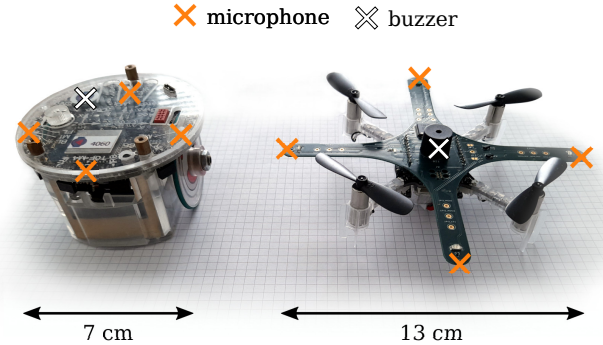


Fig. 1: The robotic platforms used for echolocation in this paper. Depicted on the left is the *e-puck* robot [9], a wheeled robot developed for education. On the right, we show the *Crazyflie* drone [7] with our custom audio extension deck, equipped with four microphones and a piezoelectric buzzer. The proposed echolocation pipeline can be used on any platform with at least one low-key microphone and sound source, respectively.

form factors than rich sensors and demand less memory for processing. Compared to proximity sensors such as infrared and ultrasound, they are less directional, allowing fewer sensors to achieve full spatial coverage. Moreover, many robots that are designed to communicate with users come equipped with microphones, and thus using audio for navigation tasks may require little additional payload.

In this paper, we develop a novel interference-based echolocation algorithm, which includes a simultaneous localization and mapping (SLAM) framework, integrating a particle filter and a factor graph [8], which accounts for the nonlinear, multimodal nature of echolocation measurements. For experimental evaluation, we develop and provide an audio extension deck for the *Crazyflie* drone. It consists of a small piezoelectric buzzer and four microphones embedded in a custom PCB, including its own microcontroller for acquisition and preprocessing. The methods developed in this paper are however applicable to any robot equipped with at least one microphone and a speaker. To underline this point, we also provide experimental validation on the ground-based *e-puck* robot [9]. Both platforms are shown in Figure 1. To summarize, our main contributions are:

- a model-based, probabilistic echolocation algorithm based on audio interference measurements,
- a combined particle filtering and SLAM pipeline suited for the non-Gaussian nature of echolocation measurements, and
- a *Crazyflie* audio extension deck with associated software for research on audio-based navigation on drones.

The paper is structured as follows. After reviewing related work in Section II, we describe our method for going from low-level audio signals to wall and robot location estimates

in Section III. In Section IV, we provide implementation details for the two used hardware platforms. In Section V, we evaluate the method on these platforms – with finely controlled motion in Section V-A, on the flying drone with one wall in Section V-B, and in a multi-wall demo in Section V-C. We conclude with a discussion of the results in Section VI.

## II. RELATED WORK

We first give an overview of existing solutions for echolocation from raw audio signals, also called the front-end in the SLAM literature [5], before going over relevant work in the back-end state estimation procedure.

*a) Sound-based front end:* Existing methods for sound-based sensing can be loosely categorized into passive solutions, which estimate the direction of arrival (DOA) of external sound sources, and active solutions, which probe the environment with an onboard sound source. While DOA for robotics is a rather active research field [10], sound-based active solutions, the focus of this paper, are considerably less explored.

Amongst the most popular active solutions are methods estimating the time of arrival (TOA) of the echoes of reflecting objects. In rooms, this information is contained in the so-called room impulse response (RIR), consisting of shifted, attenuated peaks for the early echoes, and a more noise-like reverberation tail. It can be estimated in frequency domain through the deconvolution of a known wide-band source signal and its response. When the locations of microphones and speakers are known, the first peaks of the RIR can be used to approximately recover a room’s geometry [11]. Adapting this method to a moving setup, the authors of [12] map out the room, one wall at a time, using a small loudspeaker and high-quality microphones mounted on a wheeled robot. The authors of [13] use a similar platform but recover the peaks of the RIR through nonlinear least-squares optimization on the wide-band frequency response. In follow-up work [14], this method is extended with a DOA estimator. Although promising, these methods use loudspeakers and microphones with high signal-to-noise ratio (SNR) and flat frequency responses, which is not available on the platforms studied in this paper.

The TOA of reflectors can also be determined by emitting and cross-correlating short, frequency-modulated pulses, a concept known as pulse compression. Using this technique, room geometry is estimated, using a static omnidirectional speaker and a tablet’s microphones, in [15]. Moving to a fully mobile setup, the authors of [16] perform room mapping on a smartphone. Pulse compression is also commonly used for underwater acoustic ranging [17], [18]. Note that these methods require fine control of the emitted audio pulses.

This last point is overcome by methods exploiting sound interference. The idea is to detect close-by reflectors by measuring the change in magnitude caused by interference from its echoes. In the first work bringing this idea to robotics, it was shown that a reflector can be detected based on the change in magnitude of the propeller’s ego-noise [19]. The reported results are obtained using static measurement microphones, and an offline calibration phase of the propeller’s ego noise.

The results highlight one advantage of interference-based methods: since they do not require emission of specifically designed short pulses, they can be used on noise inherent to the system.

In this paper, we take an interference-based approach. Our system is lighter compared to RIR-based methods, both in terms of hardware requirements and computing power: it runs on computationally limited platforms with simplistic speakers and low-key microphones. Compared to pulse-compression techniques, the sound signal is simpler and does not need to be exactly known — this can be an advantage when the available buzzer does not allow for fine-grained control, or when sound sources inherent to the system are used. As opposed to [19], our system does not require prior calibration, uses on-board low-key microphones and tightly integrates the motion of the device, as discussed next.

*b) Back-end state estimation:* For a practical solution, the measurements taken at subsequent times and poses need to be fused into a coherent map. This can be posed as a factor graph inference problem, where all unknown states (poses and walls) are linked by measurement factors [8]. Inference on factor graphs can become prohibitively expensive as the number of unknown states increases over time, unless certain Gaussian and sparsity assumptions are made, which is exploited by modern solvers [20], [21], [22]. While the Gaussian assumption may hold for many commonly used sensors, it does not for the sound-based front end considered in this paper: sound is known to lead to multi-modal distributions [23], [24] and thus requires different inference approaches [25], [26]. Our state estimation pipeline is most similar in nature to the work by [17], where a particle filter is used as a pre-filtering step to render the bearing and range pseudo-distributions approximately Gaussian. In our case, the particle filter helps not only reduce ambiguities, but also allows us to convert the raw path difference measurements to distance and angle estimates, which can be fed directly to the SLAM algorithm.

## III. METHODS

In this section, we describe the estimation pipeline, going from raw audio measurements to pose and plane estimates. We first derive the model of the microphone measurements as a function of the robot pose and plane in Section III-A. We derive our measurement model, which can be used to estimate the path difference, in Section III-B, and infer distance and angle distributions using discrete filtering in Section III-C. We conclude with a standard SLAM framework to jointly estimate poses and planes in Section III-D. An overview of the estimation pipeline is given in Figure 2.

### A. Derivation of signal model

We first derive the model of the individual microphone responses. A sketch of a sample setup is shown Figure 3. We place the robot’s body frame (also called the local frame) at the sound source location  $\mathbf{s} \in \mathbb{R}^2$ , and denote the  $N_m$  microphone locations in this frame by  $\mathbf{x}_m \in \mathbb{R}^2$ . The pose, consisting of the robot’s translation  $\mathbf{x}_n \in \mathbb{R}^2$  and orientation  $\phi_n \in [0, 2\pi)$

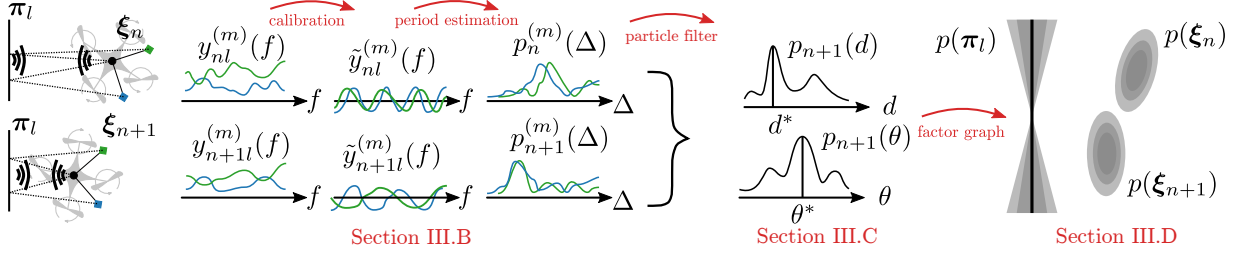


Fig. 2: Overview of estimation pipeline: we depict two microphones and their measurements in green and blue, respectively, at two subsequent poses. The raw measurements  $y_{nl}^{(m)}(f)$ , shown on the left, are used to estimate the location of nearby walls  $p(\pi_l)$  and the robot's poses over time  $p(\xi_n)$ , shown on the right.

at time  $t_n$ , is denoted by  $\xi_n$ , expressed in the fixed inertial frame (also called global frame). Considering the studied experimental platforms (a ground-based robot and a drone hovering at constant height) we operate in two dimensions, but this is not a hard requirement for the proposed solution. We denote the  $N_l$  planes by  $\pi_l$ , and we parametrize them with their global distance  $d_l$  and angle  $\theta_l$  from the origin. The recorded signal at each microphone is the sum of the direct sound and the reflected sound. Accounting for free-space attenuation and energy dissipation according to [27], it takes the form:

$$z_{nl}^{(m)}(t) := z^{(m)}(t, \xi_n, \pi_l) \quad (1)$$

$$= g^{(m)} \left( \frac{1}{4\pi\ell^{(m)}} s \left( t - \frac{\ell^{(m)}}{c} \right) + \frac{1-\rho}{4\pi r_{nl}^{(m)}} s \left( t - \frac{r_{nl}^{(m)}}{c} \right) \right),$$

where  $c$  is the speed of sound,  $\rho$  the wall absorption coefficient, and  $g^{(m)}$  the unknown, frequency-dependent, microphone gain. The lengths of the direct and reflected paths are respectively given by  $\ell^{(m)} := \|\mathbf{x}^{(m)} - \mathbf{s}\|$ , and

$$r_{nl}^{(m)} = \sqrt{(\ell^{(m)})^2 + 4(d_{nl})^2 - 4d_{nl}\ell^{(m)}\cos(\theta^{(m)} - \theta_{nl})}, \quad (2)$$

where  $\theta^{(m)} = \angle(\mathbf{x}^{(m)} - \mathbf{s})$  denotes the bearing of the  $m$ -th microphone, and  $\theta_{nl}$ ,  $d_{nl}$  denote the distance and angle of plane  $l$  as seen from pose  $\xi_n$ :

$$d_{nl} = d_l - \mathbf{x}_n^\top \mathbf{n}(\theta_l) \quad \text{and} \quad \theta_{nl} = \theta_l - \theta_n, \quad (3)$$

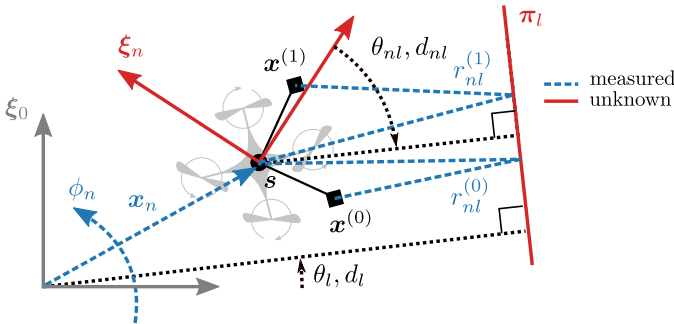


Fig. 3: Sketch of the experimental setup of echolocation with one wall, two microphones and one source. We can measure the difference between the reflected path lengths  $r_{nl}^{(m)}$  for mics  $m = 0, 1$ , and the direct path lengths  $\ell^{(m)}$ , respectively, which are related to the distance  $d_{nl}$  and angle  $\theta_{nl}$  of the wall  $\pi_l$  at pose  $\xi_n$ .

where  $\mathbf{n}(\theta)$  is a normal vector with direction  $\theta$ . Solving (2) for the distance  $d_{nl}$  given a fixed angle, we have:

$$d_{nl} := h(r_{nl}^{(m)}, \theta_l) = \frac{1}{2} \left( \ell^{(m)} \cos(\theta^{(m)} - \theta_{nl}) \right) \quad (4)$$

$$+ \sqrt{(\ell^{(m)})^2 (\cos^2(\theta^{(m)} - \theta_{nl}) - 1) + (r_{nl}^{(m)})^2},$$

which, for the limit case of a co-located phone and speaker simplifies to the widely used approximation  $d_{nl} \approx r_{nl}^{(m)}/2$ .

#### B. Interference: from audio to path differences

Next, we derive our measurement function. In the frequency domain, the squared magnitude of (1) becomes:

$$y_{nl}^{(m)}(f) = \frac{g^{(m)}(f)^2 |\hat{s}(f)|^2}{(4\pi)^2} \left( \frac{1}{\ell^{(m)2}} + \frac{(1-\rho)^2}{(r_{nl}^{(m)})^2} \right) \quad (5)$$

$$+ 2 \frac{1-\rho}{\ell^{(m)} r_{nl}^{(m)}} \underbrace{\cos\left(2\pi f(r_{nl}^{(m)} - \ell^{(m)})/c\right)}_{:= \tilde{y}_{nl}^{(m)}(f)},$$

where we introduce  $\Delta_{nl}^{(m)} := r_{nl}^{(m)} - \ell^{(m)}$  for the path difference. In theory,  $y_{nl}^{(m)}(f)$  could be used as the measurement model: evaluating it at  $N_f$  different frequencies  $f_k$ , the robot state  $\xi_n$  and wall location  $\pi_l$  can be inferred using nonlinear optimization. However, the function is highly nonlinear in the unknowns and, in particular, non-bijective, making it prone to yield ambiguous results. To make things worse, the unknown parameters  $g^{(m)}(f)$ ,  $|\hat{s}(f)|$  and  $\rho$  in (5) render the optimization problem more costly, should we try to either estimate them (thus adding more dimensions to the state vector), or marginalize them out.

Thankfully, since the ‘‘frequency’’<sup>1</sup> of the cosine in (5) depends only on the unknown state vectors and sound frequency, we can infer probability distributions of the path difference  $\Delta^{(m)}$  by studying its frequency response. We introduce  $\tilde{y}_{nl}^{(m)}(f)$  for the cosine, as shown in (5). It can be estimated from  $y_{nl}^{(m)}(f)$  through online calibration, which we will further develop in Section IV-C.<sup>2</sup>

<sup>1</sup>This ‘‘frequency’’ has the unit of seconds, and is not to be confused with the ‘‘real’’ frequencies  $f_k$  (expressed in Hz) at which we measure.

<sup>2</sup>An interesting result states that the FFT-based solution we propose is in fact equivalent to least-squares optimization with amplitude and phase of the cosine marginalized out [28].

Using a classical result from Bayesian theory, we know that the probability of a signal to be a sinusoid of frequency  $f$  is directly related to the signal's periodogram [29]. Applying this result here, the probability  $p_n^{(m)}(\Delta)$  of microphone  $m$  being at a path difference  $\Delta$  at time  $n$  is given by:

$$p_n^{(m)}(\Delta) = \eta \left[ 1 - \frac{2P_{\tilde{y}}^{(m)}(\Delta/c)}{\sum_{k=1}^{N_f} (\tilde{y}_{nl}^{(m)}(f))^2} \right]^{\frac{2-N_f}{2}}, \quad (6)$$

$$\text{with } P_{\tilde{y}}^{(m)}(f) := \frac{1}{N_f} \left| \sum_{k=1}^{N_f} \tilde{y}_{nl}^{(m)}(f) e^{j2\pi f f_k} \right|^2, \quad (7)$$

where  $\eta$  is a normalization factor. By choosing a roughly uniform spacing of frequencies, we can use the FFT of  $\tilde{y}$  to calculate  $P_{\tilde{y}}^{(m)}(f)$ . For visualization purposes, we sketch an example of  $\tilde{y}_{nl}^{(m)}(f)$ , for different frequencies and distances, in Figure 4. Intuitively speaking, we sample an approximately vertical slice of this function, and the periodicity of the slice is related to the path difference of the closest wall.

Next, we fuse multiple path difference distributions to obtain distance and angle distributions that can be fed to our SLAM framework.

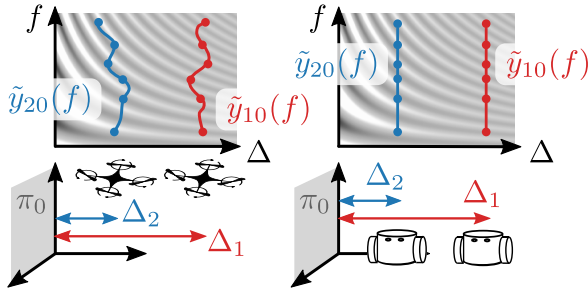


Fig. 4: Sketch of interference patterns over path differences and frequencies, with the samples recorded by a drone (left) and a ground-based robot (right). For different distances, we measure different periodicities in the interference. Note that the ground-based robot can measure clean vertical slices, as opposed to the drone.

### C. Particle filter: from path differences to planes

Because of the non-linear measurement model and the poor signal quality that common light-weight microphones and buzzers provide, the path difference distributions are subject to high noise levels and ambiguities. We propose a particle filtering approach for converting them to more unimodal distance and angle distributions. The proposed filter implicitly assumes that, for a small time window, the pose estimates are subject to only little drift, and can thus be used to resolve the ambiguities in the distributions. Mathematically speaking, we want to convert our potentially ambiguous path distributions  $p_n^{(m)}(\Delta)$ , obtained from (6), to unimodal distance- and angle distributions  $p(d_l)$  and  $p(\theta_l)$ .

a) *Initialization*: We initialize  $N_p$  particles, containing the (local) angle and distance candidates  $(d_{0,k}, \theta_{0,k})$ , with  $k = 0 \dots N_p - 1$ . The distances and angles are chosen uniformly from an area of size  $[0, d_{\max}] \times [0, 2\pi)$ . We denote by  $d_{\max}$  the maximal distance that we aim to estimate, given by the

maximally resolvable path difference.<sup>3</sup> Because of low SNR at high distances, we clip this maximal distance at 80 cm. We initialize all particles with equal weights  $w_k = 1/N_p$ .

b) *Prediction*: At each timestep, we use the current movement estimates to transform the particles to the new local coordinates:

$$\begin{aligned} d_{n,k} &= d_{n-1,k} - \mathbf{n}(\theta_{n-1,k} + \phi_n)^\top (\mathbf{x}_n - \mathbf{x}_{n-1}) \\ \theta_{n,k} &= \theta_{n-1,k} - (\phi_n - \phi_{n-1}), \end{aligned} \quad (8)$$

where  $\phi_n$  and  $\mathbf{x}_n$  are relative pose estimates. We add a fixed proportion (10%) of uniformly distributed particles, in order to prevent the filter from converging to local minima.

c) *Update*: Next, we update the particle weights using the newest measurements  $p_n^{(m)}(\Delta)$ . Using each particle's  $(d_{n,k}, \theta_{n,k})$  values, we calculate the corresponding path difference  $\Delta_k^{(m)}$  with (2) and evaluate the distributions using linear interpolation. Assuming the microphone measurements are independent, we set the value  $w_k$  to the product of the  $N_m$  probabilities thus obtained.

d) *Resampling*: After each update step, we resample the particles according to their weights, using the stratified resampling algorithm [30].

### D. Planar simultaneous localization and mapping

In the final step, we aim to feed the filtered plane measurements, along with potential pose measurements, to a SLAM framework. This ensures long-term consistency, and enables crucial tasks such as data association and path planning.

In the factor graph representation of our problem, the nodes correspond to poses and planes. The pose estimates  $\tilde{\xi}_n \in SE(d)$  are incorporated in unary factors of the form:

$$c_n = \left\| \xi_n \ominus \tilde{\xi}_n \right\|_{\Sigma_n}, \quad (9)$$

where  $\ominus$  is the difference operator defined in the Lie algebra of  $SE(d)$ , and  $\Sigma_n$  is the diagonal pose covariance matrix, fixed heuristically according to the pose estimation accuracy of the state estimator ( $\sigma_x = \sigma_y = 1$  cm,  $\sigma_\phi = 5$  deg).

For the plane measurements, we first extract distance and angle estimates  $\tilde{d}_{nl}, \tilde{\theta}_{nl}$  and standard deviations  $\sigma_{nl}^\theta, \sigma_{nl}^d$  from the particle filter, using the weighted particle mean and standard deviation. Approximating the distance and angle distributions as Gaussians, we use the binary plane factors of the form [31]:

$$c_{nl} = \left\| \begin{bmatrix} \mathbf{R}_n^\top \mathbf{n}(\theta_l) \\ \mathbf{x}_n^\top \mathbf{n}(\theta_l) \end{bmatrix} - \begin{bmatrix} \mathbf{n}(\tilde{\theta}_{nl}) \\ \tilde{d}_{nl} \end{bmatrix} \right\|_{\Sigma_{nl}}, \quad (10)$$

where  $\mathbf{R}_n$  is the rotation matrix corresponding to  $\phi_n$ .  $\Sigma_{nl}$  is the noise covariance matrix, calculated from  $\sigma_{nl}^\theta, \sigma_{nl}^d$ , with the upper-left block given by:

$$(\sigma_{nl}^\theta)^2 \frac{\partial \mathbf{n}}{\partial \theta} \Big|_{\tilde{\theta}_{nl}} \frac{\partial \mathbf{n}}{\partial \theta} \Big|_{\tilde{\theta}_{nl}}^\top. \quad (11)$$

<sup>3</sup>By the Nyquist criterion we have  $d_{\max} = h(\Delta_{\max} + \ell) = h(c/2\delta_f + \ell) \approx c/4\delta_f$ , with  $\delta_f$  the (average) difference between the sampled frequencies.

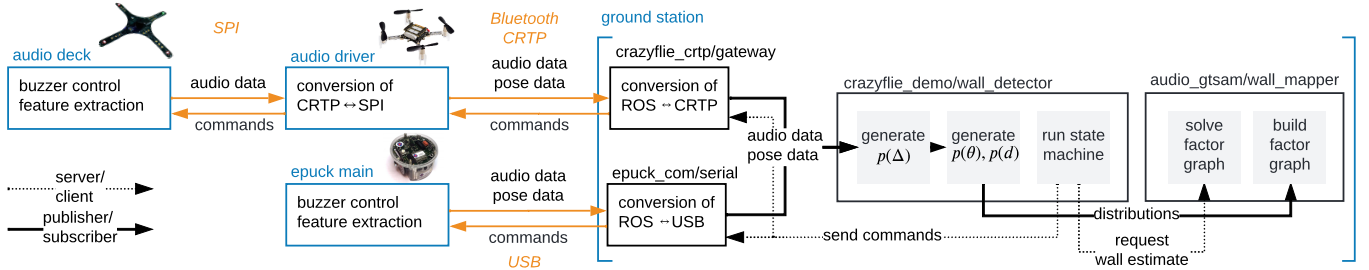


Fig. 5: Processing pipeline from firmware to the ground station’s ROS processing pipeline. The audio data and pose data is sent from either the Crazyflie drone (top row) or the e-puck robot (bottom row) to the ground station, where they are processed in parallel by a series of ROS nodes. Note that service/client connections (dotted lines) are only triggered upon request, while listener/publisher connections (solid black lines) are running continuously.

To determine whether a new measurement corresponds to a new plane or to a revisited plane, we introduce the following data association loss between planes  $\pi_i$  and  $\pi_j$ :

$$e(\pi_i, \pi_j) = \|\mathbf{n}(\theta_i)d_i - \mathbf{n}(\theta_j)d_j\|. \quad (12)$$

This loss measures how far the normal points of the two planes are from each other, thus incorporating both angle as well as distance discrepancies. We associate a new plane measurement to a previously seen plane if (12) falls below a given threshold. We found that a threshold of 30 cm performed well throughout our experiments. We solve the factor graph using the *iSAM2* solver implemented in *gtsam* [21].

#### IV. EXPERIMENTAL PLATFORMS

To demonstrate the described algorithm’s performance, the main experimental platform studied is the *Crazyflie* drone, a micro-drone with relatively poor computing resources (microcontroller STM32F405) and strict payload constraints. To fit these requirements, we design an audio-deck optimized to add little weight, and equipped with its own microcontroller (STM32F446) to offload the low-level audio pre-processing. The deck conforms with the standard format of *Crazyflie* extension decks, thus adhering to its plug-and-play philosophy. The deck contains four MEMS microphones attached to its extremities, a positioning chosen for its good trade-off between minimal propeller noise and off-centre weight. A piezoelectric buzzer, which has a reduced PCB footprint and energy consumption compared to a speaker, is placed in the centre of the deck. Note that one microphone is enough for the described algorithms, but having more microphones both increases the SNR and enables other applications such as DOA estimation. Relative pose estimates are obtained using the drone’s optical flow deck. A photo of the *Crazyflie* equipped with the audio deck is shown in Figure 1, and all hardware design files are made publicly available.<sup>4</sup>

We also test our algorithms on the wheeled *e-puck* robot (version 2) [9]. Just like the custom audio deck, the robot possesses four MEMS microphones, but it has a more versatile and louder electromagnetic speaker. Being a ground-based robot, the *e-puck* allows for the evaluation of the methods in more controlled settings, eliminating both position jitter and propeller noise. Relative pose estimates are obtained through wheel odometry.

<sup>4</sup>The code base including hardware design files and ROS pipeline is available at <https://github.com/LCAV/audioROS>.

#### A. Low-level audio processing

The full processing pipeline is visualized in Figure 5. In the firmware (left part of the plot), the signals recorded by the four microphones are first stored in buffers of size  $N = 2048$  at a sampling rate of  $F_s = 48$  kHz. With these values, the resulting frequency resolution, using the real-valued FFT, is  $\Delta_f = F_s/N \approx 23$  Hz.

The piecewise constant frequency sweep of the buzzer is generated through PWM signals. For the drone, to increase SNR, the frequency range is chosen as to be minimally affected by propeller noise under average drone hovering thrusts, while ensuring that the played frequencies match the available frequency analysis bins. Each note is played until the microphones have recorded one full buffer, which takes  $N/F_s \approx 40$  ms. For a sweep of  $N_f = 20$  discrete frequencies, this results in circa 1 s per sweep. After each sweep, the complex response is calculated through a windowed FFT, using the flattop window, which yields faithful magnitude measurements even under small frequency errors [32]. The response at the current buzzer frequency is extracted and added to an outgoing buffer.

After completion of each sweep, the next sweep is started only once the data was successfully sent to the ground station. For the *Crazyflie* drone, the buffer is passed first via SPI to the main processor and then through the custom Bluetooth protocol (CRTP) to the ground station. The data throughput of both SPI and CRTP being significantly higher than the playback rate of the sweeps  $N_f \times 2 \times 32 = 1280$  bps, we can ensure smooth transmission. For the *e-puck* robot, we omit the intermediate SPI and CRTP communication and send the audio data directly over USB to the ground station.

#### B. Ground station processing

On the ground station (right half of Figure 5), the received audio data is passed through a modular processing pipeline implementing the steps described in Sections III-B to III-D through custom nodes and interfaces, written in *python* in the Robot Operating Systems (ROS) framework, version *Galactic*. The full software suite, including a simulation framework and implementations of DOA methods, are made publicly available.

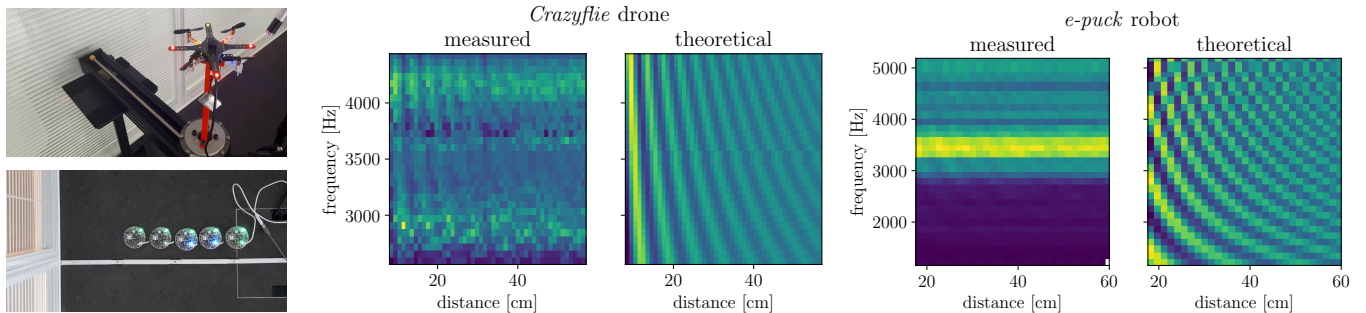


Fig. 6: Interference patterns measured at one microphone, using the drone’s stepper-motor setup and the *e-puck* setup. Photos of the experimental setups are shown to the left. Note that the measured values have the same patterns as predicted by theory, using equation (5).

### C. Online joint calibration

In our model (5), there are two unwanted and unknown, frequency-dependent gains: the highly non-linear frequency response of the piezo buzzer  $|\hat{s}(f)|$ , and the gains of the different microphones  $g^{(m)}(f)$ . If we remove these two factors, we can use the measurement model  $\tilde{y}_{nl}^{(m)}(f)$ , and path difference estimation is reduced to a simple frequency analysis, as described in III-B. Since the two unknown gains are entangled, we choose to estimate them jointly. The intuition of the calibration is the following: while the robot is moving, it measures a portion of the distance-frequency function, as visualized in Figure 4. Even for small movements, *i.e.* small variations of wall distance  $d$ , we are likely to sample both destructive and constructive interference regimes. We can thus expect that taking a moving average over a sufficiently long time window yields a good estimate of the joint speaker-microphone gain. To reduce the computational cost of the calibration, we implement the average using a simple infinite impulse response (IIR) low-pass filter:

$$\tilde{g}_n^{(m)}(f) = (1 - \lambda)\tilde{g}_{n-1}^{(m)}(f) + \lambda y_{nl}^{(m)}(f), \quad (13)$$

where we have introduced  $\tilde{g}_n^{(m)}(f)$ , the estimate of the joint gain function  $g^{(m)}(f)^2|\hat{s}(f)|^2$  at time index  $n$ . The parameter  $\lambda$  controls the effective window width, and we use a value of  $\lambda = 0.3$  throughout all experiments.

## V. RESULTS

We evaluate our systems in three increasingly difficult stages. First, we obtain fine-grained measurements of the wall’s interference patterns by moving the drone and *e-puck* robot in small steps towards the wall. For this purpose, the drone is mounted on a linear stepper motor. In a second stage, we evaluate the drone’s performance in localizing a single wall during flight, before concluding with a multi-wall demo.

### A. Stepper motor and ground-based robot

Moving the drone and *e-puck* robot in centimeter-steps perpendicular to a glass wall, we create the measured interference matrices shown in Figure 6. The frequency sweeps consist of  $N_f = 32$  uniformly spaced frequencies, where the range for the drone is chosen so as to avoid the propeller noise harmonics. We note that, although noisy, we can clearly

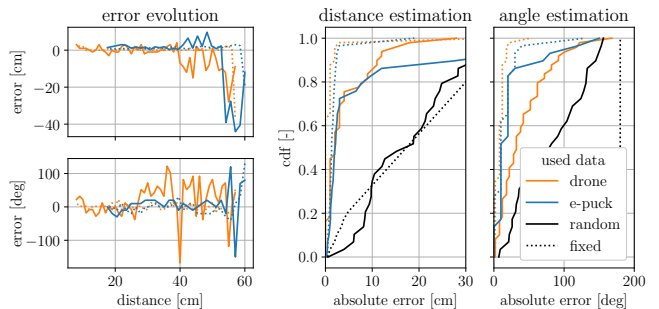


Fig. 7: Performance of distance and angle estimation. Left: distance and angle error as a function of wall distance. Right: cumulative distribution functions (cdf) of absolute errors. Shown are the experimental results from the drone on the stepper motor and the *e-puck* robot. For comparison, we also include the results using simulated data. The error using random guesses or one fixed guess serve as worse-case baselines.

discern the interference patterns predicted by theory. The pattern is particularly pronounced closer to the wall. We also note a strong frequency-dependent gain, particularly for the *e-puck* robot, which we remove through online calibration as described in Section IV-C.

Next, we apply our estimation pipeline to these measurements. Treating each frequency sweep (each column in Figure 6) separately, we evaluate the performance of both distance and angle estimation. We found that  $N_p = 400$  particles gave consistently good results throughout all experiments, with which one full estimation (including update, prediction and resampling) takes less than 75 ms. We first investigate the estimation error as we increase the distance to the wall (left plots in Figure 7). Distance estimation is reliable up to 40 cm from the wall, with the maximum error staying below 2 cm. Angle estimation is less reliable, in particular for the drone. However, up to *ca.* 30 cm, the maximum error is smaller than 20 deg. We take a closer look at the cumulative probability distributions (cdfs) in the right plots of Figure 7. As worst-case baselines, we plot the result of choosing random angles or distances, or using a fixed value at the mid-point. As best-case baseline, we run the proposed solution on simulated data. We observe that the median error for distance estimation for both *e-puck* and drone experiments is less than 3 cm. The *e-puck* robot also performs particularly well at angle estimation with a median error below 10 deg.

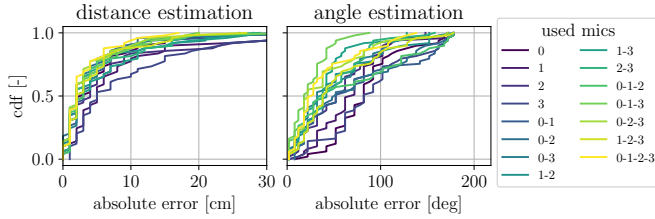


Fig. 8: Ablation study for the number of microphones used for distance and angle estimation on the drone (stepper-motor setup). While performance degrades with fewer microphones, it is still satisfactory even for a single microphone.

Finally, we perform an ablation study on the number of microphones used for estimation. Focusing on the drone results for brevity, Figure 8 shows that the performance goes down as we exclude more microphones. However, even for a single microphone, we still achieve median errors of less than 5 cm and 90 deg, which is sufficient for robust wall detection.

### B. Results on flying drone

The results thus far suggest that the proposed algorithm works well on robots with precise motion. For the remainder of this paper, we move to the more challenging setup of a flying drone. We fly the drone at constant speed towards a flat surface (glass or whiteboard), of which we estimate the location. This setup adds to the above studies the nuisance factors of 1) lateral movement during measurements and 2) varying propeller noise. To reduce both, we pick a shorter frequency sweep of  $N_f = 20$  and omit the softer middle frequencies. The results are more variable, as shown in Figure 9. The drone however still localizes the wall with a median distance error of less than 8 cm for almost all test runs. The angle estimates, on the other hand, lose in accuracy, with performances ranging from 30 deg up to 120 deg median error. One possible explanation is that the movement between two consecutive sweeps is relatively small, making angle estimation very sensitive to noise.

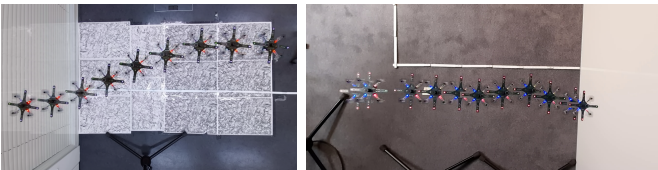
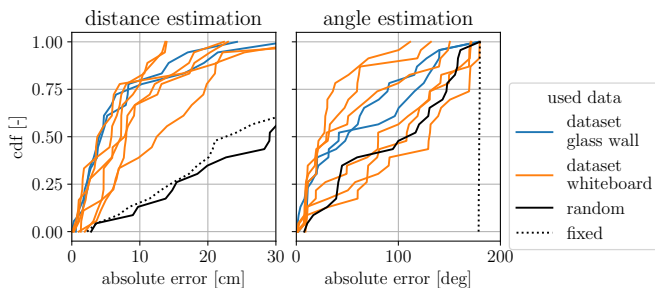


Fig. 9: Distance and angle estimation by the flying drone approaching the wall. Top: cumulative distribution functions of the absolute errors, where each line corresponds to a different experiment. The same baselines as for Figure 7 are used. Bottom: merged consecutive frames of two example experiments (bird view).

### C. Multi-wall demo

Finally, we implement a multi-wall detection demo. The drone flies back and forth between two whiteboards using only sound to detect, avoid, and map them, as shown in Figure 10. We control the drone manually, but the processing runs in real time on the recorded *bag* files.

We assume there is a wall ahead of the drone when the distance estimate is below a threshold of 20 cm. Once a wall is detected, we perform data association by (12). Because of the low accuracy of angle estimates observed in the flying experiments, we use the simplification that a detected wall is always in front of the drone with respect to its movement. The average processing time of the non-optimized *python* implementation of the factor-graph inference, is less than 1 ms, even when running on all nodes (up to 200 for the second demo). Together with the inference time from the particle filter, the state estimation can thus run at *ca.* 10 Hz.

We qualitatively evaluate the performance of the full pipeline in Figure 10, where we show the drone's pose estimates, wall estimates and ground truth wall locations. The drone successfully maps and avoids the walls, and the labelling works reliably. In particular, in the second experiment (right plot in Figure 10), new measurements are correctly associated with  $\pi_0$  when revisiting the first wall.

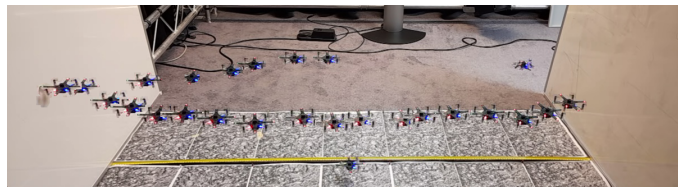
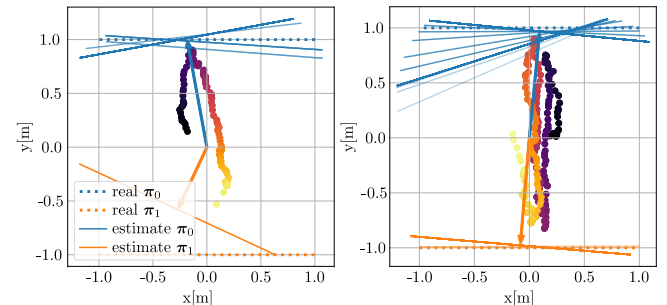


Fig. 10: Live wall avoidance experiments. Top: Estimated poses and planes after factor-graph inference, for two experiments. The positions over time are plotted in yellow to dark-blue. Wall estimates are plotted with decreasing transparency over time. Bottom: merged consecutive frames of first experiment (side view).

## VI. CONCLUSION AND FUTURE WORK

We have proposed an end-to-end system for wall localization based on audio measurements. Using our custom audio deck for the *Crazyfly* drone and the off-the-shelf *e-puck* robot, we show how an approximate interference model can be used to determine the location of a reflector. This algorithm is suited for light-weight and cheap hardware, and runs entirely in real time without prior calibration.

For ground-based robots or drones with a controlled movement, we achieve a precision of less than 2 cm and 30 deg

median error over a distance of 50 cm. For the more challenging setting of a flying drone, the accuracy lowers to *ca.* 8 cm, but the method is still able to perform wall detection reliably, which we demonstrate in a multi-wall detection demo. For the latter, the estimates are fed into a factor-graph SLAM pipeline which also performs data association.

The performance drop when moving from ground-based to flying platforms suggests that the system would benefit from more sophisticated algorithms for handling propeller noise. For example, varying propeller noise and sound interference (e.g. background noise like voices or music) may affect the performance. Adaptive frequency sweep selection based on surrounding noise bears the potential to greatly increase the generalizability and robustness of the system. Compared to distance estimation, angle estimation was found to be more sensitive to noise. In future work, we plan to add other direction indicators such as sound level or phase differences as input to the angle estimation. Furthermore, an implicit assumption of the proposed method is that the robot is static during each frequency sweep. While this is easily achieved for ground-based robots, a method more specifically targeted to drones could account for its noisy motion. Finally, to overcome the potential nuisance of audible signals, a promising direction of future research consists of replacing the buzzer signal with a system's inherent sound sources such as propeller noise.

#### ACKNOWLEDGMENTS

We would like to thank Daniel Burnier for providing the *e-puck* robot and technical support, the students Isaac, Kaourintin and Emilia for their valuable help, and Karen, Eric and Mia for their feedback on the manuscript.

#### REFERENCES

- [1] A. D. Grinnell, E. Gould, and M. B. Fenton, "A history of the study of echolocation," in *Bat Bioacoustics*, Springer Handbook of Auditory Research, Fenton, M. Brock et al., Ed. New York, NY: Springer, 2016
- [2] R. Simon, M. W. Holderied, C. U. Koch, and O. V. Helversen, "Floral acoustics : Conspicuous echoes of a dish-shaped leaf attract bat pollinators," *Science*, vol. 333, no. 6042, pp. 631–634, 2011.
- [3] D. R. Griffin and R. Galambos, "The sensory basis of obstacle avoidance by flying bats," *Journal of Experimental Zoology*, vol. 86, no. 3, pp. 481–506, 1941.
- [4] S. Greif and B. M. Siemers, "Innate recognition of water bodies in echolocating bats," *Nature Communications*, vol. 1, no. 106, pp. 1–6, 2010.
- [5] C. Cadena, L. Carlone, H. Carrillo, Y. Latif, D. Scaramuzza, J. Neira, I. Reid, and J. J. Leonard, "Past, present, and future of simultaneous localization and mapping: Toward the robust-perception age," *IEEE Transactions on Robotics*, vol. 32, no. 6, pp. 1309–1332, 2016.
- [6] C. X. Lu, S. Rosa, P. Zhao, B. Wang, C. Chen, J. A. Stankovic, N. Trigoni, A. Markham, J. A. Stankovic, N. Trigoni, and A. M. See, "See through smoke : Robust indoor mapping with low-cost mmWave radar," in *MobiSys*, 2020, pp. 14–27.
- [7] W. Giernacki, M. Skwierczyński, W. Witwicki, P. Wroński, and P. Kozierski, "Crazyflie 2.0 quadrotor as a platform for research and education in robotics and control engineering," in *22nd International Conference on Methods and Models in Automation and Robotics*, 2017, pp. 37–42.
- [8] F. Dellaert, "Factor graphs : Exploiting structure in robotics," *Annual Review of Control, Robotics and Autonomous Systems*, vol. 4, pp. 141–166, 2021.
- [9] F. Mondada, M. Bonani, X. Raemy, J. Pugh, C. Cianci, A. Klaptocz, J.-C. Zufferey, D. Floreano, and A. Martinoli, "The e-puck, a robot designed for education in engineering," in *Proceedings of the 9th Conference on Autonomous Robot Systems and Competitions*, 2009, pp. 59–65.
- [10] C. Rascon and I. Meza, "Localization of sound sources in robotics: A review," *Robotics and Autonomous Systems*, vol. 96, pp. 184–210, Oct. 2017.
- [11] I. Dokmanić, R. Parhizkar, A. Walther, Y. M. Lu, and M. Vetterli, "Acoustic echoes reveal room shape," *Proceedings of the National Academy of Sciences*, vol. 110, no. 30, pp. 12 186–12 191, 2013.
- [12] M. Kreković, I. Dokmanić, and M. Vetterli, "EchoSLAM: Simultaneous localization and mapping with acoustic echoes," in *IEEE International Conference on Acoustics, Speech and Signal Processing*, 2016, pp. 11–15.
- [13] U. Saqib and J. R. Jensen, "A model-based approach to acoustic reflector localization with a robotic platform," in *IEEE/RSJ International Conference on Intelligent Robots and Systems*, 2020, pp. 4499–4504.
- [14] —, "A framework for spatial map generation using acoustic echoes for robotic platforms," *Robotics and Autonomous Systems*, vol. 150, pp. 1–16, 2022.
- [15] O. Shih and A. Rowe, "Can a phone hear the shape of a room?" in *International Conference on Information Processing in Sensor Networks*, 2019, pp. 277–288.
- [16] B. Zhou, M. Elbadry, R. Gao, and F. Ye, "Towards scalable indoor map construction and refinement using acoustics on smartphones," *IEEE Transactions on Mobile Computing*, vol. 19, no. 1, pp. 217–230, 2020.
- [17] N. R. Rypkema, E. M. Fischell, and H. Schmidt, "One-way travel-time inverted ultra-short baseline localization for low-cost autonomous underwater vehicles," in *IEEE International Conference on Robotics and Automation*, 2017, pp. 4920–4926.
- [18] S. E. Webster, R. M. Eustice, H. Singh, and L. L. Whitcomb, "Advances in single-beacon one-way-travel-time acoustic navigation," *The International Journal of Robotics Research*, vol. 31, no. 8, pp. 935–949, 2012.
- [19] L. Calkins, J. Lingeitch, L. Mcguire, J. Geder, M. Kelly, M. M. Zavlanos, D. Sofge, and D. M. Lofaro, "Bio-inspired distance estimation using the self-induced acoustic signature of a motor-propeller system," in *IEEE International Conference on Robotics and Automation*, 2020, pp. 5047–5053.
- [20] M. Kaess, S. Member, A. Ranganathan, and S. Member, "iSAM: Incremental Smoothing and Mapping," *IEEE Transactions on Robotics*, vol. 24, no. 6, pp. 1365–1378, 2008.
- [21] M. Kaess, H. Johannsson, R. Roberts, V. Ila, J. J. Leonard, and F. Dellaert, "iSAM2: Incremental smoothing and mapping using the Bayes tree," *International Journal of Robotics Research*, vol. 31, no. 2, pp. 216–235, 2012.
- [22] T. D. Barfoot, J. R. Forbes, and D. J. Yoon, "Exactly sparse Gaussian variational inference with application to derivative-free batch nonlinear state estimation," *International Journal of Robotics Research*, vol. 39, no. 13, pp. 1473–1502, 2020.
- [23] M. Y. Cheung, D. Fourie, N. R. Rypkema, P. V. Teixeira, H. Schmidt, and J. Leonard, "Non-gaussian SLAM utilizing synthetic aperture sonar," in *IEEE International Conference on Robotics and Automation*, 2019, pp. 3457–3463.
- [24] D. Fourie, N. R. Rypkema, P. V. Teixeira, S. Claassens, E. Fischell, and J. Leonard, "Towards real-time non-gaussian SLAM for underdetermined navigation," in *IEEE/RSJ International Conference on Intelligent Robots and Systems*, 2020, pp. 4438–4445.
- [25] D. Fourie, J. Leonard, and M. Kaess, "A nonparametric belief solution to the Bayes tree," in *IEEE/RSJ International Conference on Intelligent Robots and Systems*, vol. 2016–Novem, 2016, pp. 2189–2196.
- [26] D. Fourie, "Multi-modal and inertial sensor solutions for navigation-type factor graphs," Ph.D. dissertation, Massachusetts Institute of Technology, 2017.
- [27] J. Borish, "Extension of the image model to arbitrary polyhedra," *The Journal of the Acoustical Society of America*, vol. 75, no. 6, pp. 1827–1836, 1984.
- [28] J. T. Vanderplas, "Understanding the lomb-scargle periodogram," *The Astrophysical Journal Supplement Series*, vol. 236, no. 1, p. 16, 2018.
- [29] E. T. Jaynes and G. L. Bretthorst, *Probability Theory – the Logic of Science*. Cambridge University Press, 1987.
- [30] C.-E. Särndal, B. Swensson, and J. Wretman, "Model assisted survey sampling," in *Springer Science & Business Media*, 2003, pp. 100–109.
- [31] A. J. B. Trevor, J. G. C. Rogers III, and H. I. Cristensen, "Planar surface SLAM with 3D and 2D sensors," in *IEEE International Conference on Robotics and Automation*, 2012, pp. 3041–3048.
- [32] G. Heinzl, A. Rüdiger, and R. Schilling, "Spectrum and spectral density estimation by the Discrete Fourier transform (DFT), including a comprehensive list of window functions and some new flat-top windows," *unpublished*, 2002, Accessed: Jan, 2023. [Online] Available: [https://holometer.fnal.gov/GH\\_FFT.pdf](https://holometer.fnal.gov/GH_FFT.pdf).